

# Using Geometric Graph Matching in Image Registration

Giomar O. Sequeiros Olivera<sup>1</sup><sup>a</sup>, Aura Conci<sup>2</sup><sup>b</sup> and Leandro A. F. Fernandes<sup>2</sup><sup>c</sup>

<sup>1</sup>Anhanguera Educacional, Niterói, RJ, Brazil

<sup>2</sup>Institute of Computing, Fluminense Federal University, Niterói, RJ, Brazil

**Keywords:** Image Registration, Graph Matching, Edit Distance, Infrared Images.

**Abstract:** Image registration is a fundamental task in many medical applications, allowing interpreting and analyzing images acquired using different technologies, from different viewpoints, or at different times. The image registration task is particularly challenging when the images have little high-frequency information and when average brightness changes over time, as is the case with infrared breast exams acquired using a dynamic protocol. This paper presents a new method for registering these images, where each one is represented in a compact form by a geometric graph, and the registration is done by comparing graphs. The application of the proposed technique consists of five stages: (i) pre-process the infrared breast image; (ii) extract the internal linear structures that characterize arteries, vascular structures, and other hot regions; (iii) create a geometric graph to represent such structures; (iv) perform structure registration by comparing graphs; and (v) estimate the transformation function. The Dice coefficient, Jaccard index, and total overlap agreement measure are considered to evaluate the results' quality. The output obtained on a public database of infrared breast images is compared against SURF interest points for image registration and a state of the art approach for infrared breast image registration from the literature. The analyzes show that the proposed method outperforms others.

## 1 INTRODUCTION

Medical image processing has become a fundamental tool in healthcare, being increasingly used in tasks such as diagnostic, treatment planning, surgeries, and disease follow-up (Rahman, 2018). In medical image-based applications, it is often interesting to analyze more than one set of data simultaneously since images obtained with different acquisition technologies may reveal complementary information about structures of interest (Balakrishnan et al., 2018). Moreover, same patient images taken at different times can help to monitor abnormalities or assist their treatment. In both cases, image registration (IR) is an essential task in the processing of medical images, being crucial in all applications that need to combine, compare, or merge visual information (Brock et al., 2017; Conci et al., 2015; González et al., 2018).

The IR process consists of estimating a function that allows mapping one of the images to the other (Zitová and Flusser, 2003). For this purpose, a wide variety of IR techniques can be seen in the

literature, that in general are divided into intensity-based and feature-based methods (Zitová and Flusser, 2003). For the second approaches, it is necessary to manually, semi-automatically, or automatically extract feature points from the images (Ma et al., 2016). The manual and semi-automatic selection of feature points are usually time-consuming and often impractical. Consequently, it is important to develop techniques that allow the automatic identification of these points. Moreover, those techniques must be stable to ensure consistency and reproduction of the results. Unfortunately, the most used approaches for automatic identification of feature points in natural images are not adequate for IR of low contrast images such as infrared images (a.k.a. thermograms or thermal images) (Falco et al., 2020). Similarly, some approaches use anatomical structures present in the medical images to perform the registration (Deng et al., 2010). When applied to infrared breast images, the problem in this type of IR approach is to represent the anatomical structures properly. In this sense, geometric graphs emerge as a powerful tool to represent objects and their spatial relationships (Garcia-Guevara et al., 2018). Graph matching has been applied in several domains to solve problems such as data retrieval,

<sup>a</sup>  <https://orcid.org/0000-0002-7172-6525>

<sup>b</sup>  <https://orcid.org/0000-0003-0782-2501>

<sup>c</sup>  <https://orcid.org/0000-0001-8491-793X>

graph classification, pattern discovery, and structural data characterization (Pinheiro et al., 2017) but are still little explored for IR (Tong et al., 2017).

In this paper, we present a method for extracting the location of internal linear structures from infrared breast images and represent them as geometric graphs. The internal linear structures may be arteries, vascular structures, or hot regions. We also present an algorithm to match the graph representations of the structures extracted from two images. The proposed matching procedure is an adaptation of the edit distance (Armiti and Gertz, 2014) that, in addition to considering the structural relationships of a vertex and its neighbors, uses local image descriptors around the edge that connects two vertices to improve the matching. We have applied this proposition for registering breast examinations and have observed significant advantages when compared it to previous techniques.

The remaining of this paper is organized as follows: Section 2 presents a literature review of related works. The proposed approach is detailed in Section 3. Section 4 presents the experiments and their results. Finally, Section 5 concludes the paper and points to directions for future exploration.

## 2 RELATED WORK

There are few approaches in the literature for breast infrared IR. To the best of our knowledge, none of them uses graph-based techniques to perform the task. Thus, we claim that this is one of the original contributions of our work. Next, we discuss some works that extend traditional IR methods to thermograms.

Agostini et al. (2009) recorded about 500 frames of thermal images. Prior acquisition, they glued black and white markers of 5mm diameter on the patient's skin. The white markers are used for estimating the transformations between image pairs, while the black markers are used to measure the quality of the method. The alignment of the set of frames is performed by taking the first image of the sequence as the reference, being the others transformed to it. Since the white markers guide registration, the method begins with the automatic identification of this kind of marker. After that, each marker is manually labeled and used to solve the linear transformation that better explains their location in the image pair. The efficacy of this method is measured by the signal-to-noise ratio (SNR). In this case, the signal analyzed along the series is formed by the temperatures in the positions of the black markers in the first frame, together with the temperature of the same positions in the other images. The noise calculated by the measurement is

characterized by the change throughout the series of the temperature values in the observed locations.

Lee et al. (2010) also proposed the IR of infrared images by using markers previously placed on the patient. These markers are automatically identified by the Harris' corners detection method (Harris and Stephens, 1988). After that, the association between markers in both images is manually set by the user. Through these association, a transformation by Thin Plate Spline function (Holden, 2008) is calculated and used to align the sensitive to the reference image. In the end, the transformation function is refined by the simplex method. In subsequent work, Lee et al. (2012) used the Harris corner coefficient to detect feature points from heat patterns on the thermal images. Registration is made by taking the first image as a reference and estimating transformations that explain the location of the feature points on other image of the set. To evaluate the proposed approach, numbered markers were placed on a patient, and a sequence of ten images of that patient was acquired. During the acquisition, the patients are instructed to perform small movements, simulating the displacements that occur in examinations that take large time intervals.

Silva et al. (2016) used an IR process as part of a methodology that aims to analyze thermograms using time series. In their methodology, thermograms are sequentially acquired, forming a set of twenty images per patient. During the five minutes of acquisitions, the patient performs small involuntary movements for breathing. These movements lead to differences from one thermogram to another. In Silva et al. (2016) work, the first thermogram of the sequence is considered the reference image, and the others are deemed sensitive images. Thus, for the examination of a patient, the registration process is executed nineteen times since the sensitive thermograms of the sequence must be registered to the first one. Silva et al. (2016) technique uses Mutual Information (MI) as a global measure of similarity of pixel intensities to estimate translation, rotation, and scale transformations between the images.

Falco et al. (2020) used the same dataset of Silva et al. (2016) for IR. All the serial thermograms of the same patient are analyzed, creating a relationship among them. The reference image for registration is chosen as the one that is more similar to all the others. Then, all the other thermograms of a patient are registered systematically, creating a new and more similar set of thermograms. Initially, the images to be registered are classified as a reference or sensitive image. After that, all images are processed to estimate the silhouette of the patient's body. Through the silhouette, feature points are identified. These points are used to

estimate the transformation that better explains the location of the feature points from one image to another. With these transformations, a new set of serial images are created, one for each type of transformation computed. Finally, the generated images are compared with the reference image, and the set of registered images that presented the best result is chosen as the output of the registration method.

It is important to note that the techniques mentioned above either rely on markers to perform the registration or local information that may change from one image to another, such as the infrared intensity or the patient's silhouette. Our approach, on the other hand, performs the registration based on the topological relationship between the main sources of heat identified in the image, which are related to the arteries, vascular structures, and other hot regions.

### 3 THE PROPOSED APPROACH

Our method for infrared breast IR consists of five steps: (i) pre-process a given infrared breast image; (ii) extract the internal linear structures; (iii) represent the internal structures using a geometric graph; (iv) perform graph matching to register the graph of the current image to the graph of another thermogram; and (v) estimate the transformation for image registration. The following subsections describe these steps.

#### 3.1 Pre-processing

Infrared images are formed by a temperature matrix representing the thermal pixel values. By using a min-max mapping, temperatures values may be represented in the  $[0, 255]$  range as a conventional 8-bit grayscale image. Such an image can also be treated as a heightmap, i.e., the gray intensity value assigned at pixel location  $(x, y)$  also represents the distance of displacement or elevation of a surface, with 0 (black) representing minimum height and 255 (white) representing maximum height. Figures 1 (a) and (b) exemplify, respectively, an infrared breast image and the region enclosed by the rectangle in (a) represented as a relief. When the whole image is considered, the highest portions of the terrain are the warmest regions of the patient's body, with part of the ridges indicating the location of thicker blood vessels. Global minimum regions correspond to the background, i.e., areas outside the patient's body.

The purpose of the pre-processing step is to prepare the image to facilitate the extraction of internal linear structures in the next step. According to our experience, global minimum and more accentuated

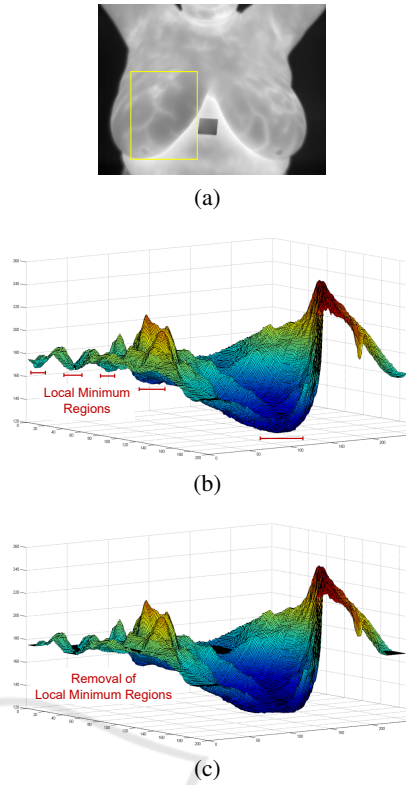


Figure 1: Three-Dimensional representation of the yellow portion of a thermogram (a) as a height map before (b) and after (c) applying the H-minima transform. Notice that the relief around local minimum in (b) have changed in (c).

local minima affect the quality of the segmentation algorithm that is used in the next step to extract internal linear structures. To solve this problem, we apply the H-minima transform (Ismail et al., 2016) as a pre-processing to suppresses all minima in the grayscale image whose intensity is less than  $h$ . Figures 1 (b) and (c) illustrate the relief induced by the thermogram before and after the application of the H-minima transform. Through empirical experimentation, we observed that the value  $h = 8$  meets the needs of the proposed technique.

#### 3.2 Extraction of Linear Structures

The input of this step is the image resulting from the pre-processing stage. The result is a binary image where 1-pixels represent the location of the internal linear structures, which correspond to ridges of the relief induced by the thermogram.

In this work, we use the watershed algorithm by flooding (Kornilov and Safonov, 2018) to achieve the objective of the internal linear structures' extraction step. This algorithm simulates relief flooding from water sources located at local minimum. When the

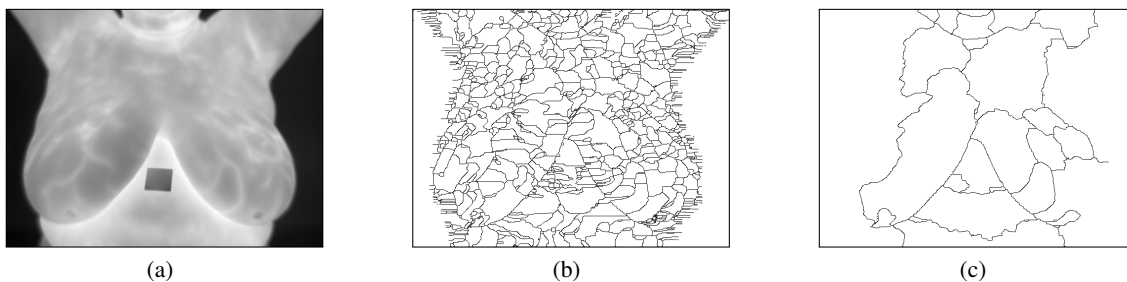


Figure 2: From left to right: (a) the original thermogram; (b) internal structures for (a); and (c) internal structures for the image resulting from the H-minima transform of (a).

water rises, retention basins are created. At the end of the flooding process, neighboring basins define the watershed lines. Figure 2 (b) shows the watershed of the non pre-processed gray-level image in Figure 2 (a). As it is possible to observe, many lines were defined as the internal linear structures because many retention basins were created. Figure 2 (c) shows the result of the watershed segmentation applied to the version of Figure 2 (a) pre-processed by the H-minima transform. This result presents a much cleaner set of linear features.

The binary image produced by the watershed algorithm is subsequently processed by the thinning procedure described by Zhang and Suen (1984). The objective is to obtain a binary image with structures having the thickness of one pixel.

### 3.3 Linear Structure Representation

Once the internal structure is extracted, it must be turned into a geometric graph. For this, we start with an 8-connected neighborhood representation of the binary image obtained in the previous step.

Let  $G = (V, E)$  be an undirected graph, where  $V$  is the set of vertices and  $E$  the set of edges. The vertices  $v \in V$  correspond to the 1-pixels of the given binary image, and the 8-connected neighborhood of 1-pixels defines the edges  $e = (v_i, v_j) \in E$  for any pair of neighbor vertices  $v_i, v_j \in V$ . The graph is geometric because vertices carry the  $(x, y)$  pixels' location, and edges' weight is given by the Euclidean distance between the pixels of the vertices that define them. Thus, the weight of an edge can be equal to 1 or  $\sqrt{2}$ .

One problem that arises in representing the internal linear structures using  $G$  is the creation of too many vertices, which can compromise the performance of matching algorithms (Zheng et al., 2013). To mitigate this issue, we create the geometric graph  $G' = (V', E')$  from the graph  $G = (V, E)$ . Here,  $V' \subseteq V$  is the new set of vertices formed by endpoints, corners, and junction points of the linear structures in the given binary image. The new set of edges

$E' \subseteq V' \times V'$  allows connecting vertices in  $V'$  considering the shortest paths in  $V$ . Additionally, the new graph is enhanced with the inclusion of features at the vertices and edges. Below we describe the processes for obtaining the new sets of vertices and edges, and how to extract the features to be assigned to elements of the new graph.

**Determination of the New Set of Vertices.** The candidate vertices for graph  $G' = (V', E')$  must satisfy one of the three rules below:

1.  $v \in V$  is an endpoint, i.e.,  $degree(v) = 1$ ;
2.  $v \in V$  is a corner, i.e.,  $degree(v) = 2$  and the vertex  $v$  and its direct neighbors are not collinear;
3.  $v \in V$  is a junction point, i.e.,  $degree(v) \geq 3$ ;

where  $degree(v)$  is the number of vertices directly connected to  $v$ . To avoid creating many close vertices in  $G'$ , we only include in  $V'$  the candidate vertices that do not have another candidate vertex within a radius bounded by the threshold  $d$ . In our experiments, we observed that the value  $d = 20$  meets the needs of the proposed technique for the image database we have using. This value must be adjusted for other databases regarding the resolution of the input thermograms and the patient's distance to the camera.

**Determination of the New Set of Edges.** The set of edges  $E$  becomes obsolete when the new collection  $V'$  of vertices is defined as a subset of  $V$ . Therefore, we need to build  $E'$  to reconnect the vertices that were included in the graph  $G'$ . We use the graph  $G$  in this process to not lose the overall structure of the linear features depicted in the input binary image. More specifically, we create edges  $e' = (v'_i, v'_j) \in E'$  using the Dijkstra algorithm to determine the shortest path between  $v'_i$  and  $v'_j$  in the original graph  $G$ . An edge is created whenever there is no vertex in  $V'$  positioned between vertices  $v'_i$  and  $v'_j$  in such path.

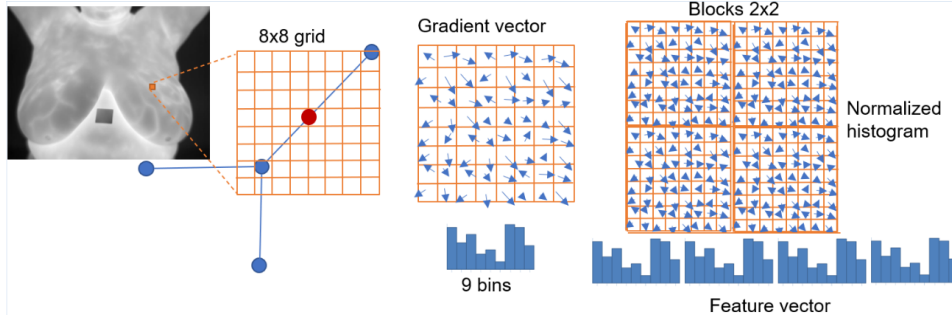


Figure 3: Example of visual feature extraction.

**Feature Extraction.** The purpose of this step is to create spatial features vectors and visual feature vectors for the elements in the geometric graph  $G'$ .

Spatial features are associated with vertices. For a given vertex  $v' \in V'$ , its spatial features are encoded by a cyclic string of tuples,  $F = [f_1, f_2, \dots, f_n]$ , where  $n = \text{degree}(v')$  and  $f_i$  is a tuple  $(|e'_i|, \angle e'_i e'_{i-1})$ . Here,  $|e'_i|$  represents the length of the edge  $e_i = (v', v'_i)$ , where  $v'_i$  is the neighbor vertex reached from  $v$  through  $e_i$ , and  $\angle e'_i e'_{i-1}$  denotes the angle between the edges  $e'_i$  and  $e'_{i-1}$  in counterclockwise order.

Visual feature vectors are created to encode visual information around the graph edges. For this purpose, we use Histogram of Oriented Gradients (HOG) features (Dalal and Triggs, 2005), generally applied in pattern recognition and image processing to detect or recognize objects. In the present case, the objects represent variations of intensities nearby the thicker blood vessels in the original infrared breast image.

We compute one HOG feature from the  $8 \times 8$  grid placed at the center point of each edge of the graph  $G'$ . The cells in this grid are grouped into  $2 \times 2$  blocks, and the orientation of the gradients of each pixel of the image is transformed in such a way that they are mapped to the  $[-180^\circ, 180^\circ)$  range, with a  $40^\circ$  interval, i.e., the orientations assume values in the discrete set  $\{-180^\circ, -140^\circ, -100^\circ, -60^\circ, -20^\circ, 20^\circ, 60^\circ, 100^\circ, 140^\circ\}$ . After this process, the magnitude of each pixel is used as a weighting factor for calculating the average orientation of each cell. Finally, each block is represented by a histogram of average orientations. Histograms of 9 bins are created, and since we have 4 blocks, the whole feature vector will have size 36. Figure 3 illustrates the computation of the HOG features.

### 3.4 Graph Matching

This step aims to perform the comparison of graphs  $G'$  and  $F'$  representing, respectively, the reference and the sensitive images, to obtain the best correspondence between their vertices. From this correspon-

dence, it will be possible to estimate the transformation that will allow registering the thermograms.

Algorithm 1 estimates the resulting matching matrix. We use the Hungarian method (Riesen et al., 2018) to find the best matching between the vertices of  $G'$  and  $F'$  from the matrix  $M$ , whose entry  $M_{i,j}$  represents the cost of transforming the information related to the  $i$ -th vertex  $v' \in G'$  into the information assigned to the  $j$ -th vertex  $u' \in F'$  (see Algorithm 2).

The vertex transformation cost is computed by Algorithm 3 as the vertex edit distance (Armiti and Gertz, 2014). Editing distance is a measure of similarity and represents a powerful approach within error-tolerant methods for correspondence between graphs. This distance involves basic operations such as removing, adding, or replacing vertices and edges. This distance is calculated using dynamic programming with complexity  $O(nm^2)$ , where  $n = \text{degree}(v')$  and  $m = \text{degree}(u')$  (Armiti and Gertz, 2014). We implement the substitution, insertion, and removal operations applied in the edit distance algorithms following Armiti and Gertz (2014).

The following are the edit operations on the edges: *substitution*, *insertion*, and *removal*. Given two vertices  $v$  and  $u$ , let be the edge  $e_i$  the neighbor of  $v$  and the edge  $e_j$  the neighbor of  $u$ . The substitution cost between two edges is defined as:

$$\gamma(e_i \rightarrow e_j) = d_L(e_i, e_j) + d_S(e_i, e_j), \quad (1)$$

where  $d_L(e_i, e_j)$  returns the Euclidean distance be-

---

Algorithm 1: Geometric graph matching.

---

```

1 SetAlFnt
   Input: Graphs  $G' = (V', E')$  and  $F' = (U', D')$ 
   Output: The matching matrix
2 foreach  $v' \in V'$  do
3    $i \leftarrow$  the index of  $v'$ ;
4   foreach  $u' \in U'$  do
5      $j \leftarrow$  the index of  $u'$ ;
6      $M_{i,j} \leftarrow \text{computeMinimalDistance}(v', u')$ ;
7 return  $\text{HungarianMethod}(M)$ ;

```

---

tween the visual features of the edges  $e_i$  and  $e_j$  that were extracted by using HOG features. Similarly,  $d_S(e_i, e_j)$  returns the spatial distance based on angles and length of the edges:

$$d_S(e_i, e_j) = \begin{cases} c(e_i, e_j) & , \text{ for } |\theta_{e_i} - \theta_{e_j}| \leq \pi, \\ c(e_i, e_j) + 2 \max\{l_{e_i}, l_{e_j}\} & , \text{ otherwise,} \end{cases} \quad (2)$$

where

$$c(e_i, e_j) = \sqrt{l_{e_i}^2 + l_{e_j}^2 - 2l_{e_i}l_{e_j} \cos(|\theta_{e_i} - \theta_{e_j}|)}, \quad (3)$$

and  $\theta_{e_k}$  is the angle between an edge and the previous one and  $l_{e_k}$  is the length of the edge.

The cost of substitution is defined as the distance required so that the neighboring vertex of the edge  $e_i$  is aligned with the neighboring vertex of the edge  $e_j$ , which can be seen as the polar distance between them. The cost for insertion and removal operations are defined by:

$$\gamma(\lambda \rightarrow e_i) = \gamma(e_i \rightarrow \lambda) = \begin{cases} c(e_i) + d_L(e_i) & , \text{ for } \theta_{e_i} \leq \pi, \\ c(e_i) + 2l_{e_i} + d_L(e_i) & , \text{ otherwise,} \end{cases} \quad (4)$$

where

$$c(e_i) = \sqrt{l_{e_i} + l_{e_{i-1}} - 2l_{e_i}l_{e_{i-1}} \cos(|\theta_{e_i}|)}. \quad (5)$$

### 3.5 Image Registration

In this work, we assume that the transformation used to register the sensitive image to the reference image is a planar homography. The result of the previous step is the best match between the vertices of two geometric graphs representing thermograms. In some cases, incorrect matches (outliers) may occur, introducing errors in the homography that would be estimated if all corresponding vertices were considered. Consequently, the image registration step uses the RANSAC algorithm (Fischler and Bolles, 1981) to remove outliers and estimate the best homography between the actual corresponding vertices (inliers). The resulting transformation function serves to change the sensitive image, making it more similar to the reference one. For this, it is necessary to use interpolation techniques that map the continuous values of the transformation function into discrete values of the image representation domain (Pan et al., 2012).

## 4 EXPERIMENTS AND RESULTS

Following Falco et al. (2020) and Silva et al. (2015), a sample from the DMR-IR database (Silva et al., 2016)

Algorithm 2: Compute minimal distance.

---

```

1 SetAlFnt
   Input: Vertices  $v'$  and  $u'$ 
   Output: minimal distance
2  $word1 \leftarrow$  spatial and visual features from  $v'$ ;
3  $word2 \leftarrow$  spatial and visual features from  $u'$ ;
4  $n \leftarrow degree(v')$ ;
5  $m \leftarrow degree(u')$ ;
6 if  $n < m$  then
7    $\swarrow$  swap( $word1, word2$ );
8  $minimalDistance \leftarrow \infty$ ;
9 for  $i \leftarrow 1$  to  $m$  do
10    $word2 \leftarrow rotate(word2)$ ;
11    $distance \leftarrow editDistance(word1, word2)$ ;
12   if  $distance > minimalDistance$  then
13      $\swarrow$   $minimalDistance \leftarrow distance$ ;
14 return  $minimalDistance$ ;

```

---

Algorithm 3: Edit distance.

---

```

1 SetAlFnt
   Input: Spatial and visual features
    $word1$  and  $word2$ 
   Output: The edit distance stored in  $D_{n+1, m+1}$ 
2  $n \leftarrow length(word1)$ ;
3  $m \leftarrow length(word2)$ ;
4 for  $i \leftarrow 1$  to  $n$  do
5    $\swarrow$   $D_{i,1} \leftarrow i$ ;
6 for  $j \leftarrow 1$  to  $m$  do
7    $\swarrow$   $D_{1,j} \leftarrow j$ ;
8 for  $i \leftarrow 1$  to  $n$  do
9    $c1 \leftarrow$  the  $i$ -th entry of  $word1$ ;
10  for  $j \leftarrow 1$  to  $m$  do
11     $c2 \leftarrow$  the  $j$ -th entry of  $word2$ ;
12    if  $c1 = c2$  then
13       $D_{i+1, j+1} \leftarrow D_{i, j}$ ;
14    else
15       $D_{i+1, j+1} \leftarrow \min\{$ 
16         $D_{i, j} + SubstitutionCost(c1, c2),$ 
17         $D_{i, j+1} + InsertRemoveCost(c1, c2),$ 
18         $D_{i+1, j} + InsertRemoveCost(c1, c2)\}$ ;
19  return  $D_{n+1, m+1}$ ;

```

---

was used to carry out the experiments and to validate the proposed approach. From these, 11 healthy patients and 12 with disease diagnoses were selected due their diversity of body shapes. Each one has a set of 20 frontal images captured every 15 seconds during 5 minutes according to a protocol proposed by Silva et al. (2016). This time is long enough for the patient to perform involuntary movements in such a way that becomes necessary the IR before analysis.

We have considered the first thermogram of each patient as the reference image, and the remaining 19 thermograms have been considered the sensitive images that will be registered to the first one. Due to

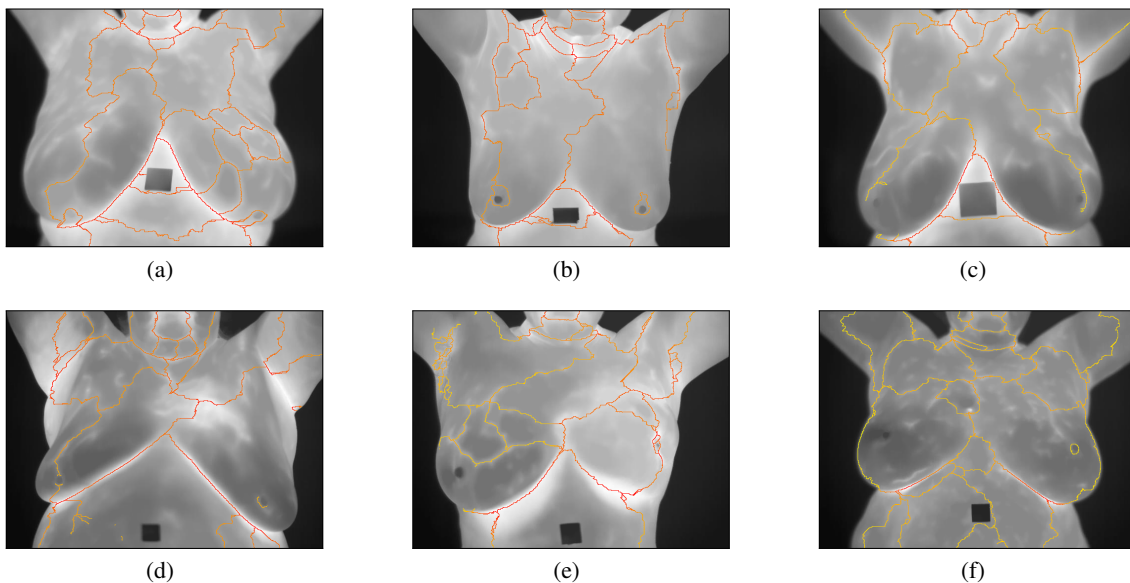


Figure 4: Examples of structures extracted from thermograms of healthy patients (a)-(c), and from thermograms of patients diagnosed with a disease in the breast (d)-(f).

the non-deterministic nature of the RANSAC algorithm, we have performed the registration of each pair of images ten times. We have considered the average transformation as the expected transformation. By doing so, we avoid small variations from one registration to another in the same pair of images. Thus, having 23 patients with 20 images each,  $19 \times 10 = 190$  RANSAC evaluations were performed per patient, leading to a total of 4,370 registrations.

For simplicity, through this section, the patients are identified by the numbering P1, P2, ..., P23. Patients P1 to P11 correspond to those with healthy breasts, while patients P12 to P23 present some breast disease diagnoses. Figure 4 shows the linear structures (orange lines) extracted from some of such images, of which Figures 4 (a)-(c) are from healthy patients, and Figures 4 (d)-(f) are from breast disease patients. It is important to mention that each image shown in Figure 4 represents the first in a series of 20 images acquired by using a dynamic protocol proposed by Silva et al. (2016). The diagnoses were obtained through other exams (mammography or biopsy) and the visual differences are not necessarily evident enough to distinguish between healthy and diseased patients by analysing just one thermogram. An example of visual differences between healthy and diseased patients is the presence of asymmetries heat distribution in the left and right breast. Figure 5 shows the geometric graphs defined from the linear structures presented in Figure 4.

Next, we discuss the complexity of the geometric graphs constructed using the proposed approach and

two other suggested solutions, the performance of the proposed technique in the registration of images of each patient, and its performance comparison to other IR techniques.

**Number of Vertices.** Table 1 compares the average number and the standard deviation (SD) of the number of vertices in three types of geometric graphs computed per patient's condition on images of the dataset used in our experiments. Recall that we are considering 23 patients, with 20 images each, making 460 geometric graphs, where 220 are related to healthy patients, and 240 are related to patients with some breast disease.

In Table 1, the graph type N-8 considers the binary image representing the thermogram's watershed structure as a graph where each 1-pixel is a vertex. The 8-connectivity between pixels defines edges of length 1 or  $\sqrt{2}$ . In graph type Harris, the Harris corner detector (Harris and Stephens, 1988) was applied to the watershed image to identify the graph's ver-

Table 1: Average and standard deviation (SD) of the number of vertices per patient's condition.

Condition	Measure	Graph Type		
		N-8	Harris	Ours
Healthy	Average	3319.55	422.73	173.27
	SD	477.67	58.22	25.02
With Disease	Average	4039.25	523.00	209.75
	SD	825.86	104.71	43.45

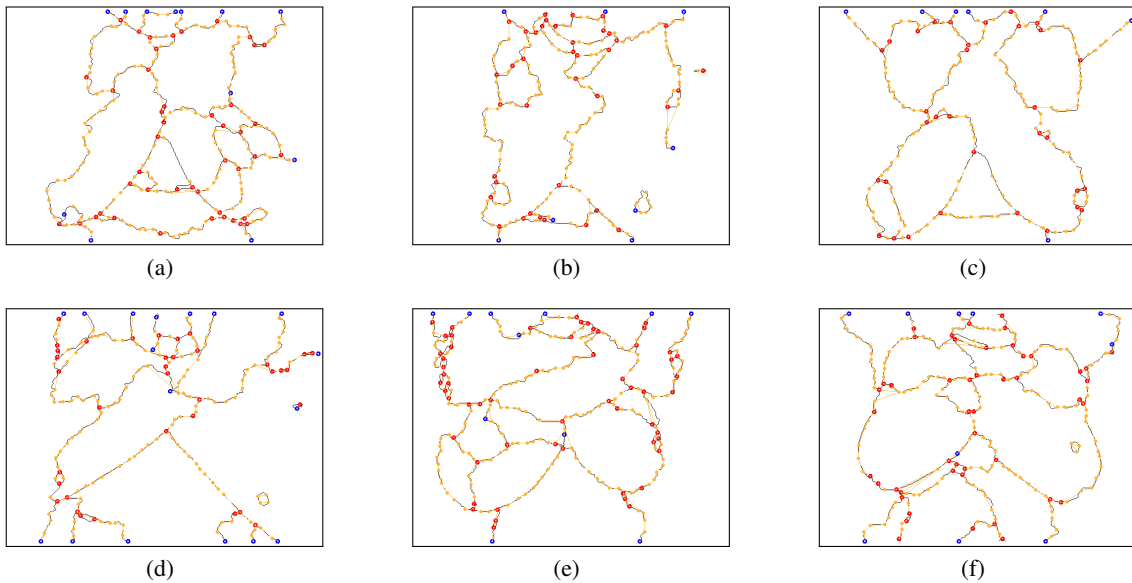


Figure 5: Geometric graphs computed from the thermograms presented in Figure 4. Blue, orange and red vertices correspond to vertices created from, respectively, endpoints, corners, and junction points.

tices as the detected points of interest. Notice that the average number and the SD of vertices produced by the proposed approach is much smaller than the values resulting from graphs of type N-8 and Harris. It is necessary to have about 173 vertices on average to represent the internal structures of the thermogram with healthy diagnosis and 210 vertices for patients with some disease. The importance of having a small number of vertices to represent the structures properly resides in the fact that graph matching algorithms are NP-complete (Riesen et al., 2018). Thus, be able to describe the structures present in the thermograms with less information is a desirable property of the proposed approach. Such a property allows obtaining a considerable computational performance gain in the execution of graph matching algorithms.

The Dice coefficient is defined as:

$$Dice = \frac{2N(I_R \cap I_S)}{N(I_R) + N(I_S)}, \quad (6)$$

where  $I_R$  and  $I_S$  are the binary representation of, respectively, the reference and sensitive images. These binary images are considered as sets whose elements are the pixels that form the patient’s body. Here,  $N(S)$  is the number of elements in the set  $S$ . Thus, it gives the area of the objects formed by 1-pixels in the given image, that can be seen in Figure 6. To that extent, Dice coefficient equal to 1 means the total overlap, the greater similarity between the images, while 0 means no overlap.

The Jaccard index represents the percentage of

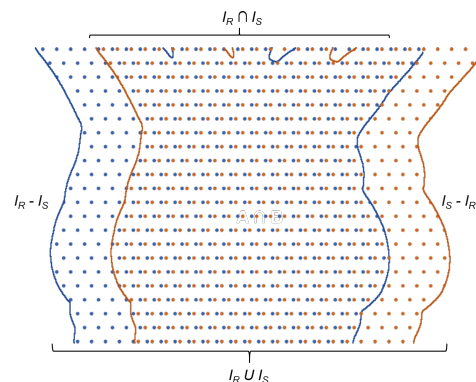


Figure 6: Comparison between reference image  $I_R$  and sensitive image  $I_S$ .

**Performance of the Registration.** Table 2 presents the performance of the proposed graph-based IR approach per patient. The analysis considers the mean Dice coefficient (Dice, 1945), mean Jaccard index (Jaccard, 1912), and mean Total Overlap Agreement (TOA) measure (Klein et al., 2009) achieved before and after registration. Table 2 also presents the number of times in which the evaluation measure gets improved after IR. These values have been highlighted for convenience. Similarly, Table 3 shows the standard deviation per patient before and after registration. In this case, the increments of standard deviation after registration are highlighted, and they indicate greater dispersion in relation to the mean.

Table 2: Mean performance results per patient before and after using the proposed IR technique.

Healthy Patient	Dice		Jaccard		TOA	
	Before	After	Before	After	Before	After
P1	0.97275	0.98511	0.98617	0.99249	0.98528	0.98879
P2	0.88114	0.92625	0.93563	0.96160	0.94110	0.94836
P3	0.92052	0.95638	0.95836	0.97766	0.96167	0.98204
P4	0.91520	0.91190	0.95534	0.95379	0.96774	0.93614
P5	0.97410	0.98584	0.98684	0.99285	0.98311	0.99066
P6	0.96601	0.97545	0.98269	0.98755	0.98795	0.98357
P7	0.90388	0.96251	0.94897	0.98082	0.94532	0.97394
P8	0.94357	0.97285	0.97094	0.98592	0.96495	0.97987
P9	0.94280	0.97477	0.97034	0.98720	0.96922	0.98075
P10	0.95459	0.97377	0.97674	0.98670	0.96572	0.98209
P11	0.97641	0.96841	0.98805	0.98393	0.98979	0.97793
<b>Improved/Subjects</b>	9/11		9/11		8/11	

Patient with Disease	Dice		Jaccard		TOA	
	Before	After	Before	After	Before	After
P12	0.97569	0.97634	0.98768	0.98770	0.98209	0.98256
P13	0.91645	0.94692	0.95610	0.97266	0.95920	0.95609
P14	0.93368	0.95948	0.96537	0.97926	0.96919	0.98325
P15	0.97468	0.96117	0.98717	0.98008	0.98828	0.97179
P16	0.97230	0.95491	0.98593	0.97682	0.98993	0.97251
P17	0.97370	0.97787	0.98665	0.98879	0.97607	0.98210
P18	0.96957	0.96970	0.98454	0.98456	0.98576	0.98474
P19	0.93046	0.92758	0.96385	0.96236	0.96490	0.94261
P20	0.97691	0.96566	0.98831	0.98251	0.99157	0.97271
P21	0.94886	0.95382	0.97348	0.97582	0.97446	0.96801
P22	0.96275	0.96974	0.98098	0.98461	0.97918	0.97741
P23	0.97168	0.97826	0.98561	0.98900	0.98915	0.98338
<b>Improved/Subjects</b>	8/12		8/12		3/12	
<b>Total Improved/Subjects</b>	17/23		17/23		11/23	

overlap of two sets in relation to their union:

$$Jaccard = \frac{N(I_R \cap I_S)}{N(I_R \cup I_S)}. \quad (7)$$

Like the Dice coefficient, Jaccard index equal to 1 means greater similarity between the images, while 0 indicates no similarities.

The TOA measure for a given registration is:

$$TOA = \frac{N(I_R \cap I_S)}{N(I_S)}, \quad (8)$$

whose value also range from 0 to 1.

We have used similarity measures based on binary images following works in the literature. This allows our technique to be compared with other approaches. Besides, the intensity information on the patient's thermographs varies over time because of the dynamic protocol (Silva et al., 2016). This variation can introduce errors in the analysis when the intensities are compared directly after registration.

From Table 2, it is possible to observe that, according to the Dice coefficient and Jaccard index, the proposed IR approach improved the registration of images of 9 out of 11 healthy patients and 8 out of 12 patients with a disease. For the Dice coefficient, the evaluation measure values increased up to 0.0586 units in success cases (subject P7) and decreased up to 0.0174 units in the other cases (subject P16). For the Jaccard index and TOA measure, the most significant performance improvement was of 0.0166 (subject P13) and 0.0286 units (subject P7), respectively, while the greatest deterioration in performances were of, respectively, 0.0091 (subject P16) and 0.0316 units (subject P4). These results show that the benefits of the proposed technique outweigh the problems it may introduce.

From a more detailed look at the registration results, it was observed that, in a general way, the proposed method performed well, achieving IR improvements in 77% of the pairs of images of healthy pa-

Table 3: Standard deviation performance results per patient before and after using the proposed IR technique.

Patient	Dice		Jaccard		TOA	
	Before	After	Before	After	Before	After
P1	0.00654	0.00581	0.00335	0.00295	0.00356	0.00457
P2	0.06300	0.02134	0.03744	0.01144	0.04407	0.01878
P3	0.03094	0.01257	0.01684	0.00660	0.01693	0.00767
P4	0.03740	0.02177	0.02067	0.01183	0.02031	0.01820
P5	0.01336	0.00924	0.00687	0.00472	0.00900	0.00800
P6	0.00877	0.01035	0.00452	0.00531	0.00704	0.00891
P7	0.04465	0.01687	0.02453	0.00880	0.02387	0.01480
P8	0.01067	0.03501	0.00563	0.01864	0.00800	0.02189
P9	0.02912	0.01002	0.01548	0.00515	0.01553	0.00883
P10	0.01141	0.00614	0.05970	0.00315	0.00693	0.00473
P11	0.00673	0.00861	0.03440	0.00443	0.00400	0.00686
P12	0.00797	0.03590	0.00410	0.01940	0.00593	0.03573
P13	0.03378	0.01736	0.01834	0.00909	0.01549	0.01522
P14	0.03536	0.01510	0.01943	0.00795	0.02024	0.00935
P15	0.00676	0.02167	0.00346	0.01128	0.00233	0.01748
P16	0.00859	0.02164	0.00441	0.01148	0.00308	0.01165
P17	0.00904	0.00939	0.00463	0.00485	0.00889	0.00797
P18	0.00826	0.01486	0.00426	0.00776	0.00411	0.00570
P19	0.02218	0.01626	0.01194	0.00874	0.01467	0.01506
P20	0.00600	0.00853	0.00308	0.00442	0.00344	0.00757
P21	0.03275	0.04485	0.17470	0.02512	0.01858	0.02642
P22	0.01191	0.01046	0.00615	0.00537	0.00748	0.00869
P23	0.01000	0.00592	0.00517	0.00302	0.00436	0.00614
<b>Total Improved/Subjects</b>	14/23		16/23		10/23	

tients. In the case of patients with diseases, there were improvement in 56% of the image pairs.

Figures 7 (a) and (b) exemplify, respectively, the reference image and 19<sup>th</sup> sensitive image for patient P1. Figure 7 (c) shows the pixelwise difference between (a) and (b) without performing IR, while Figure 7 (d) shows the difference after performing the proposed IR technique. In both images (c) and (d), darker and lighter regions correspond to more significant (signed) differences. Results were mapped to the  $[0, 255]$  range to improve visualization. A noticeable superposition improvement can be observed after IR, where most of the image (d) takes a medium gray tone, which represents a difference close to zero.

**Processing Time.** The testbed implementation of our approach was not tailored for performance. Even so, it is capable of performing image registration in less than one second on a PC with Intel Core i5 6500 CPU and 8GB of RAM.

**Comparison to Other Approaches.** Figure 8 shows a summary of the performance achieved by the proposed method, the method described by Falco et al. (2020), and the traditional use of SURF to execute IR. As one can see, SURF performed worse, not being competitive with either of the other two

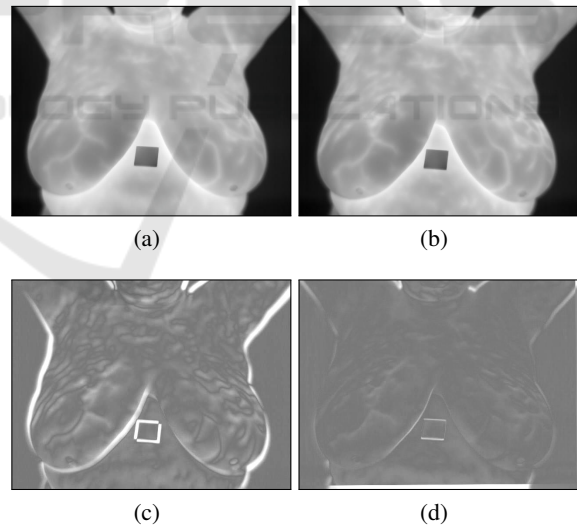


Figure 7: Example of a thermogram taken as the reference image (a) and the 19<sup>th</sup> sensitive image (b) of a given patient. Images (c) and (d) show the normalized pixel by pixel difference between images (a) and (b) before and after applying the proposed IR technique, respectively.

techniques. It is because SURF and related feature extraction techniques, e.g., SIFT and ORB, require high-frequency information to characterize textured regions properly. By using the Dice coefficient as the

evaluation measure, our method performs better registering of healthy patients in 9 out of 11 cases, against 2 out of 11 cases where Falco's et al. approach performed better (Figure 8, a). For the Jaccard index, the mean performance of our approach was higher for 8 against 3 subjects. The TOA measure shows a score of 6 against 5 cases of better performance of the proposed technique over Falco's et al. approach. When patients with a disease are considered, results show that the Falco et al. method is slightly superior (Figure 8, b). But considering all subjects (Figure 8, c), our approach is superior in two of the three evaluation measures assumed.

## 5 CONCLUSIONS

This paper proposed an automatic method for infrared breast IR by using a geometric graph matching approach. The graph that was created has a reduced number of vertices that make it computationally efficient. The execution of our registration method performed well, especially in healthy patients. In these patients, the temperature change during the dynamic image acquisition protocol seems to be more stable. On the other hand, in patients with breast disease, more significant changes were observed in the apparent internal linear structures, leading to substantial changes in the graphs' structure and, consequently, affecting the matching process. Nevertheless, the results presented in this paper are interesting since they indicate that the first technique to use graphs for infrared breasts IR is promising.

Several works may emerge from the proposed approach. For instance, it is possible to modify the edit distance model to assign different weights to the insert, replace, and remove operations to allow different priorities to be set to the operations.

Another possible direction of future work is using other types of visual features to characterize the local information around a vertex or an edge, including the use of features extracted by artificial neural networks.

Finally, our approach could be adapted to different types of medical images with linear and vascular structures such as fundus images widely used to diagnose ocular diseases or diseases that have global effects on the vascular system (Bhatkalkar et al., 2020).

## ACKNOWLEDGEMENTS

The Brazilian research agency CAPES sponsored Giomar O. S. Olivera. Aura Conci is partially supported by MACC-INCT, CNPq (grants

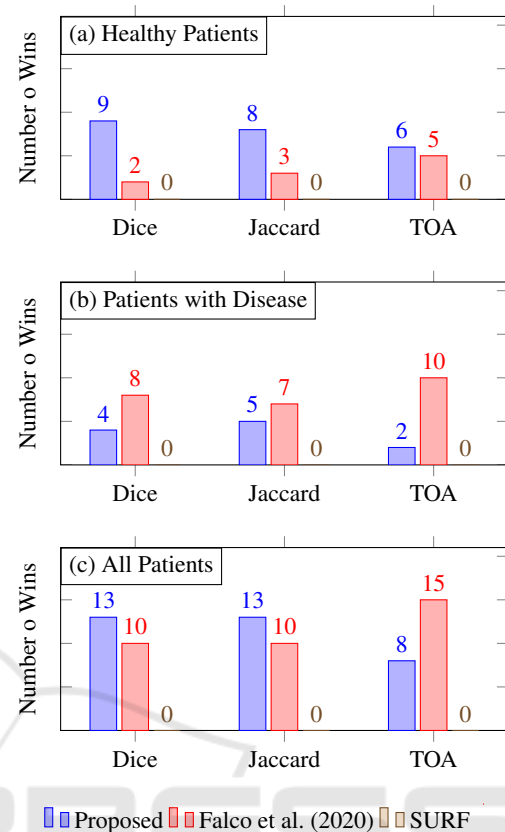


Figure 8: Summary of the comparison of results for healthy patients, patients with breast disease, and the total number of patients using the proposed approach, the IR technique described by Falco et al. (2020), and SURF.

402988/2016-7 and 305416/2018-9), and FAPERJ (project SIAD-2 and 210.019/2020). Leandro A. F. Fernandes is partially supported by the Brazilian research agencies CNPq (grant 424507/2018-8) and FAPERJ (grant E-26/202.718/2018).

## REFERENCES

- Agostini, V., Knäflitz, M., and Molinari, F. (2009). Motion artifact reduction in breast dynamic infrared imaging. *IEEE Trans. Biomedical Engineering*, 56(3):903–906.
- Armiti, A. and Gertz, M. (2014). Vertex similarity - a basic framework for matching geometric graphs. In *Proceedings of the LWA*, pages 111–122.
- Balakrishnan, G., Zhao, A., Sabuncu, M. R., Guttag, J., and Dalca, A. V. (2018). An unsupervised learning model for deformable medical image registration. In *Proceedings of the IEEE Conference on Computer Vision and Pattern Recognition*, pages 9252–9260.
- Bhatkalkar, B., Joshi, A., Prabhu, S., and Bhandary, S. (2020). Automated fundus image quality assessment

- and segmentation of optic disc using convolutional neural networks. *International Journal of Electrical & Computer Engineering*, 10:2088–8708.
- Brock, K. K., Mutic, S., McNutt, T. R., and H. Li and, M. L. K. (2017). Use of image registration and fusion algorithms and techniques in radiotherapy: report of the AAPM Radiation Therapy Committee Task Group No. 132. *Medical Physics*, 44(7):43–76.
- Conci, A., Galvão, S. S., Sequeiros, G. O., Saade, D. C., and MacHenry, T. A. (2015). A new measure for comparing biomedical regions of interest in segmentation of digital images. *Discrete Appl. Math.*, 197:103–113.
- Dalal, N. and Triggs, B. (2005). Histograms of oriented gradients for human detection. In *Proceedings of the IEEE Conference on Computer Vision and Pattern Recognition*, pages 886–893.
- Deng, K., Tian, J., Zheng, J., Zhang, X., Dai, X., and Xu, M. (2010). Retinal fundus image registration via vascular structure graph matching. *International Journal of Biomedical Imaging*, 2010:906067.
- Dice, L. R. (1945). Measures of the amount of ecologic association between species. *Ecology*, 26(3):297–302.
- Falco, A. D., Galvão, S., and Conci, A. (2020). A non linear registration without the use of the brightness constancy hypothesis. In *Proc. Intern. Conference Systems, Signals and Image Processing*, pages 27–32.
- Fischler, M. A. and Bolles, R. C. (1981). Random sample consensus: a paradigm for model fitting with applications to image analysis and automated cartography. *Communications of the ACM*, 24(6):381–395.
- Garcia-Guevara, J., Peterlik, I., Berger, M. O., and Cotin, S. (2018). Biomechanics-based graph matching for augmented CT-CBCT. *International Journal of Computer Assisted Radiology and Surgery*, 13(6):805–813.
- González, J. R., Pupo, Y., Hernandez, M., Conci, A., Machenry, T., and Fiirst, W. (2018). On image registration for study of thyroid disorders by infrared exams. In *Proc. Intern. Conf. Image Proc., Computer Vision, & Pattern Recognition*, pages 151–158.
- Harris, C. and Stephens, M. (1988). A combined corner and edge detector. In *Proceedings of the Alvey Vision Conference*, pages 147–151.
- Holden, M. (2008). A review of geometric transformations for nonrigid body registration. *IEEE Transactions on Medical Imaging*, 27(1):111–28.
- Ismail, N. H. F., Zaini, T. R. M., Jaafar, M., and Pin, N. C. (2016). H-minima transform for segmentation of structured surface. In *Proceedings of the MATEC Web of Conferences*, page 25.
- Jaccard, P. (1912). The distribution of the flora in the alpine zone. *New Phytologist*, 11(2):37–50.
- Klein, A., Andersson, J., Ardekani, B. A., Ashburner, J., Avants, B., Chiang, M. C., Christensen, G. E., Collins, D. L., Gee, J., Hellier, P., Song, J. H., Jenkinson, M., Lepage, C., Rueckert, D., Thompson, P., Vercauteren, T., Woods, R. P., Mann, J. J., and Parsey, R. V. (2009). Evaluation of 14 nonlinear deformation algorithms applied to human brain MRI registration. *NeuroImage*, 49(3):786–802.
- Kornilov, A. and Safonov, I. (2018). An overview of watershed algorithm implementations in open source libraries. *Journal of Imaging*, 4(10):123.
- Lee, C., Chang, Z., Lee, W., Lee, S., Chen, C., Chang, Y., and Huang, C. (2012). Longitudinal registration for breast IR image without markers. In *Proceedings of the International Conference on Quantitative InfraRed Thermography*.
- Lee, C., Chuang, C. C., Chang, Z. W., Lee, W. J., Lee, C. Y., C. S., Lee, Huang, C. S., Chang, Y. C., and Chen, C. M. (2010). Quantitative dual-spectrum infrared approach for breast cancer detection. In *Proceedings of the International Conference on Quantitative InfraRed Thermography*.
- Ma, J., Zhao, J., and Yuille, A. L. (2016). Non-rigid point set registration by preserving global and local structures. *IEEE Trans. Image Processing*, 25(1):53–64.
- Pan, M. S., Yang, X. L., and Tang, J. T. (2012). Research on interpolation methods in medical image processing. *Journal of Medical Systems*, 36(2):777–807.
- Pinheiro, M. A., Kybic, J., and Fua, P. (2017). Geometric graph matching using Monte Carlo tree search. *IEEE Transactions on Pattern Analysis and Machine Intelligence*, 39(11):2171–2185.
- Rahman, M. M. (2018). Literature-based biomedical image retrieval with multimodal query expansion and data fusion based on relevance feedback (RF). In *Proc. Intern. Conference Image Processing, Computer Vision, & Pattern Recognition*, pages 103–107.
- Riesen, K., Fischer, A., and Bunke, H. (2018). On the impact of using utilities rather than costs for graph matching. *Neural Processing Letters*, 48(2):691–707.
- Silva, L. F., Santos, A. A., Bravo, R. S., Silva, A. C., Muchaluat-Saade, D. C., and Conci, A. (2016). Hybrid analysis for indicating patients with breast cancer using temperature time series. *Computer Methods and Programs in Biomedicine*, 130:142–153.
- Silva, L. F., Sequeiros, G., Santos, M. L., Fontes, C. A. P., Muchaluat-Saade, D., and Conci, A. (2015). Thermal signal analysis for breast cancer risk verification. *Studies in Health Technology and Informatics*, 216:746–50.
- Tong, Y., Udupa, J. K., Ciesielski, K. C., Wu, C., McDonough, J. M., Mong, D. A., and Campbell Jr, R. M. (2017). Retrospective 4D MR image construction from free-breathing slice acquisitions: a novel graph-based approach. *Medical Image Analysis*, 35:345–359.
- Zhang, T. Y. and Suen, C. Y. (1984). A fast parallel algorithm for thinning digital patterns. *Communications of the ACM*, 27(3):236–239.
- Zheng, W., Zou, L., Lian, X., Wang, D., and Zhao, D. (2013). Graph similarity search with edit distance constraint in large graph databases. In *Proceedings of the ACM International Conference on Information & Knowledge Management*, pages 1595–1600.
- Zitová, B. and Flusser, J. (2003). Image registration methods: a survey. *Image and Vision Computing*, 21(11):977–1000.